REPORT DOCUMENTATION PAGE

Form Approved
OMB No. 0704-0188

1. AGENCY USE ONLY (Leave Blank)	2. REPORT DATE	3. REPORT TYPE AND DATES COVERED
	June 1994	Conference Proceeding

4. TITLE AND SUBTITLE
Hartmann Sensor and Dynamic Tomographical Analysis of Organized Structure.

5. FUNDING NUMBERS

6. AUTHOR(S)
L. McMackin, J. Wissler, N. Clark, E. Chen, K. Bishop, R. Pierson, B. Staveley

7. PERFORMING ORGANIZATION NAME(S) AND ADDRESS(ES)
Phillips Laboratory
3550 Aberdeen Av SE
Kirtland AFB, NM 87117-5776

8. PERFORMING ORGANIZATION REPORT NUMBER
PL-LI 94-25

9. SPONSORING / MONITORING AGENCY NAME(S) AND ADDRESS(ES)

10. SPONSORING / MONITORING AGENCY REPORT NUMBER

11. SUPPLEMENTARY NOTES
COSATI CODE(S): 20/04

12a. DISTRIBUTION / AVAILABILITY STATEMENT
Pub. in AIAA 94-2548, 18th AIAA Aerospace Ground Testing Conference, 20-23 June 1994, Colorado Springs, Colorado.

12b. DISTRIBUTION CODE
A

13. ABSTRACT (Maximum 200 words)
In the Aero-optics research program currently underway at the Phillips Laboratory, we are examining the relationship between the organized structure in the near-field region of an axisymmetric jet and the degradation of an optical field that propagates through the jet shear layer. We are developing an experimental capability in which dynamic tomographical analysis enables us to reconstruct a time series of flow-field images while simultaneously recording the optical phase incurred along many paths through the flow. From such simultaneous information we can infer relevant flow structures. In this paper we present an analysis of the one-dimensional Hartmann sensing technique with which we intend to make time-resolved tomographic measurements. We discuss the sensitivity and noise characteristics of the sensor and present novel, high resolution, measurements of flow-field structure that have been obtained from Hartmann sensor measurements. Additionally, computed tomographic reconstructions of flow-field cross-sections are created using information from the Hartmann sensor measurements. We employ these simulations to analyze the expected quality of time-resolved tomographic reconstructions and to create an optimized design of an experimental dynamic tomographic system based on Hartmann sensing.

14. SUBJECT TERMS
Hartmann sensor; tomography; flow fields; organized structure; jet shear layer; optical field

15. NUMBER OF PAGES
8

16. PRICE CODE

17. SECURITY CLASSIFICATION OF REPORT	18. SECURITY CLASSIFICATION OF THIS PAGE	19. SECURITY CLASSIFICATION OF ABSTRACT	20. LIMITATION OF ABSTRACT
Unclassified	Unclassified	Unclassified	SAR

PL-LI 94-25

AIAA 94-2548
Hartmann Sensor and Dynamic Tomographical Analysis of Organized Structure in Flow Fields

L. McMackin, J. Wissler,
N. Clark, E. Chen, K. Bishop,
R. Pierson, B. Staveley
Phillips Laboratory
Kirtland AFB, NM

18th AIAA Aerospace Ground Testing Conference

June 20-23, 1994 / Colorado Springs, CO

HARTMANN SENSOR AND DYNAMIC TOMOGRAPHICAL ANALYSIS OF ORGANIZED STRUCTURE IN FLOW FIELDS

L. McMackin, J. B. Wissler†, B. Masson‡, N. Clark
USAF Phillips Laboratory
Kirtland AFB, NM 87117

E. Chen, K. Bishop, R. Pierson
Applied Technology Associates, Inc.
Albuquerque, NM 87117

B. Staveley
University of New Mexico
Albuquerque, NM 87131

Abstract

In the Aero-optics basic research program currently underway at the Phillips Laboratory, we are examining the relationship between organized structure in the near-field region of an axisymmetric jet and the degradation of an optical field that propagates through the jet shear layer. We are developing an experimental capability in which dynamic tomographic analysis enables us to reconstruct a time series of flow-field images while simultaneously recording the optical phase incurred along many paths through the flow. From such simultaneous information we can infer relevant flow structures. In this paper we present an analysis of the one-dimensional Hartmann sensing technique with which we intend to make time-resolved tomographic measurements. We discuss the sensitivity and noise characteristics of the sensor and present novel, high-resolution measurements of flow-field structure that have been obtained from Hartmann sensor measurements. Additionally, computed tomographic reconstructions of flow-field cross sections are created using information from the Hartmann sensor measurements. We employ these simulations to analyze the expected quality of time-resolved tomographic reconstructions and to create an optimized design of an experimental dynamic tomographic system based on Hartmann sensing.

1. Introduction.

The presence of organized structure in flow fields has been the subject of much discussion in the literature since 1974.[1-5] Recently, the need for the investigation of structure in flow fields and turbulence has become more apparent due to the failure in some cases of traditional statistical methods to fully characterize atmospheric measurements[6-8]. A study of organized structure is also necessary to describe the effects on the optical performance of boundary layers, shear flows and other inhomogeneous flows[9-12] in laser transmission and imaging applications.

Investigating the effects of organized, temporally evolving flow structure on laser propagation and imaging requires the simultaneous acquisition of data delimiting the flow structure as well as data defining the optical wavefront distortions caused by the structure. Because the flow field structure evolves in time, a more complete understanding of the optical effects of organized structure can be obtained from temporally resolved measurements; in essence, a high speed movie of flow structure with its corresponding "soundtrack" of optical aberrations can be achieved with optical tomography.

Optical tomography has been used previously to create three-dimensional (3D) flow field visualizations[13-18]. However, the information collected to produce these tomographic reconstructions is usually collected over a period of time that is long with respect to the convective time-scale of flow structures. This results in a time-averaged reconstruction of the flow where images of the instantaneous structures have been smeared out.

We propose a 2D optical tomographic system that can operate at several KHz providing simultaneous flow-field structure data and wavefront measurements. High spatial resolution is achieved in the wavefront measurements and the tomographic reconstructions using Hartmann sensing techniques. High temporal resolution is obtained by limiting the data acquisition to linear measurements in a single plane.

This paper begins with a brief introduction to tomography and Hartmann sensing in Section 2. Section 3 describes the experimental apparatus used to generate the flow field and the construction of the Hartmann sensor. In Section 4 the sensitivity and the noise characteristics of the Hartmann sensor are described. Section 5 presents flow-field measurements using the Hartmann sensor and anemometry. Finally in Section 6 results of an optical tomography simulation

†Maj USAF, Senior Member AIAA,
‡Member AIAA

are presented to determine the optimal design of a fast experimental tomographic system for the investigation of flow field structure.

2. Optical tomography and Hartmann sensing.

Tomography is an inverse problem of reconstructing an image from a set of line integrals made through the object. The data obtained in a medical tomographic scan are measurements of the x-ray transmission through a two-dimensional (2D) slice of the body. The data obtained in the aero-optical tomography problem considered here are measurements of the optical phase of monochromatic laser transmission through a 2D slice of the flow-field (in a plane perpendicular to the flow direction) as shown in Fig. 1. Referring to Fig. 1, the optical phase, Φ, incurred by a single optical ray traversing a phase object with refractive index n(x,y) (i.e., the 2D slice of the flow) is given by

$$\Phi = \int_{path,s} n\,ds, \qquad (1)$$

where s is the path of the ray. A set of path-integrated phase measurements made in a particular direction, ϕ, through the flow is called a projection. The infinite set of all (noiseless) projections in all possible directions through the flow in a single plane is the Radon transform[19] of that 2D slice of its refractive index. In the notation of Fig. 1, the Radon transform of a flow field cross section given by n(x,y) is written,

$$\Phi(p,\phi) = \iint n(x,y)\,\delta(p - x\cos\phi - y\sin\phi)\,dx\,dy. \qquad (2)$$

where ϕ is the angle between axis p and the x axis, δ is the Dirac delta function and p is the position along the projection. The inverse problem of reconstructing the 2D slice from the set of one-dimensional (1D) projections is the inverse Radon transform. Under even the best experimental conditions, the data will be limited in angular extent, spatial resolution and will contain noise. Therefore, the inverse problem becomes ill-posed. The task, then, of any implementation of tomography is to produce the best reconstruction from the available data.

There are a wide variety of algorithmic implementations of the inverse Radon transform[20,21] which can be divided into several broad categories including direct inversion, Fourier or convolution techniques, and iterative techniques. It has been shown that the methods most effective for reconstructing images from data sets that are limited in angular extent, number of projections or both are iterative reconstruction techniques[22]. The algebraic reconstruction technique (ART), an iterative technique which is used in our studies, has been investigated thoroughly[23,24] and the mathematics will not be reiterated here. Briefly, ART compares projections taken through the current image iteration to the original projection data. The error in the iteration projections is backprojected along the current iteration to produce the next iteration. The iterative process continues until some minimum projection error threshold is reached

In our experiments linear (1D) Hartmann sensors will be used to obtain the optical phase data that comprises the set of 1D projections. A Hartmann sensor consists simply of an array of small cylindrical kinoform lenses (40 lenslets per inch), a CCD camera, and an algorithm that can locate centroids from the intensity pattern recorded by the camera. As shown in Fig. 2, the sensor works on the principle that the focused spots in the focal plane of the lenslet array will be deflected away from their optical axes by a distance, Δ_i, that is proportional to the local derivative of the wavefront impinging on the lenslet array.[25] Because light propagates in the direction normal to the wavefront, the local derivative, or slope of the wavefront incident on a lenslet, given by angle θ_i, determines the local direction of propagation of the light to the focal plane. In this way Δ_i is related to θ_i by

$$\tan\theta_i \approx \theta_i = \frac{\Delta_i}{f_L} \qquad (3)$$

where f_L is the focal length of the lenslets. Thus, detecting the centroid position of the spot from each lenslet measures the gradient of the optical phase along x that by simple integration yields the optical phase of a projection.

As an optical flow field investigation tool, Hartmann sensing[26] is a variant of the thin beam deflection technique used extensively to measure flow dynamics.[27-29] However, unlike the thin beam jitter technique, the sensitivity of the Hartmann measurement can be controlled. Because the magnitude of the deflection of the focal spots is directly proportional to the focal length of the lenslets (see Eq. (3)), an appropriate choice of the focal length can match the necessary sensitivity. Another advantage of the Hartmann sensor is the ability to make a large number of separate jitter measurements from a single expanded optical beam simply as a result of the small size and closely packed arrangement of the lenslets in a 1D or 2D array. Accurate tracking of flow convection and evolution of structures in the flow from measurements from a single linear Hartmann array is presented in Section 4 as a high resolution extension of thin beam jitter analysis.

For tomography, a number of linear Hartmann sensors are arranged around the circumference of the jet to measure all phase projections at different angles simultaneously (Fig. 3). Because the projections are limited to 1D and the number of projections is limited to the number that can physically fit around the flow field, the total amount of data taken is relatively low and the projection sets can be taken at high speed, at least several KHz. However, because limited amounts of data are taken, the burden of producing high quality tomographic reconstructions falls on the clever use of iterative reconstruction techniques as well as some basic knowledge about the plane of the flow to be imaged. For instance, an average size of the internal refractive index structures within the slice would indicate the necessary resolution of the tomographic system and help determine the number of projections and subapertures in each projection; upper and lower bounds on the magnitude of the index differences within the slice, the noise present in each measurement and the noise produced by the centroiding and phase reconstruction algorithms are also useful pieces of information. The effect of limited data and noise on the tomographic reconstructions are included in the tomographic simulation discussion in Section 6.

3. Experimental apparatus.

The experimental apparatus used to generate the flow-field is shown in Fig. 4. A small blower pumps room air into a duct, across heater vanes and into a plenum chamber. Heated air then flows out of the 18" x 18" x 36" plenum through a series of screens and honeycomb and into a 9-to-1 contraction section that forms the 1-inch diameter jet opening. The jet is oriented vertically and positioned in the center of custom designed optical table that allows unobstructed access around the flow at all angles. The average center velocity of the flow used in the experiments is approximately 5 m/s. The average temperature of the air in the jet is approximately 30 degrees C above ambient. The flow can be described by a Reynolds number of about 8000. The Richardson number, which is a measure of the ratio of buoyant to kinetic energy in the flow, of 0.007 indicates that buoyancy effects are negligible.[30]

Figure 5 shows the results of a velocity, U, and temperature, T, survey across the jet several stations downstream from the nozzle. The profiles are fairly flat although some rounded edges are caused by the thermal mass of the solid aluminum contraction section, which remained at ambient room temperature during the measurements. A visualization of the flow-field obtained by a horizontal smoke wire is shown in Fig. 6. Photographic flash illumination of the smoke produced by heating an oil-coated wire that is placed across the nozzle exit reveals the instantaneous structure of the interfaces between hot and cold air in a vertical planar cross section of the flow. The visualization shows that vortical flow structures caused by instabilities in the mixing layer are well developed and organized and occur in the transition region between 1 and 4 diameters downstream. The optical measurements discussed in this paper were made at an optical axis position of 2.5 diameters downstream.

The 1D Hartmann sensor used in our experiments is a two-component system consisting of a 1D lithographically-produced array of cylindrical lenslets and a 1D CCD array that is located at the back focal plane of the lenslets.[31,32] The inch-long lenslet array contains 40 lenslets of focal length, F = 10 cm, with no dead space in between (0.635 mm per lenslet). The lenslets serve to divide a single expanded laser beam into 40 sub-apertures each of which is focused onto a 50-pixel window of the 2048-pixel CCD array. A spot-locating algorithm is used to detect the position of each of the 40 focal spots within their 50-pixel window. Streamwise orientation of the inch-long linear sensor centered at an optical axis of 2.5 diameters above the nozzle opening allows high resolution detection of the vortical train at a rate of 2.2 KHz when a 5 MHz data acquisition board is used.

4. Wavefront tilt measurement sensitivity and noise characteristics of the Hartmann sensor.

In this section we examine sources of wavefront sensor error and present a measurement of the sensitivity of the 1D Hartmann sensor. The accuracy of wavefront measurements made with Hartmann sensors is limited by noise sources associated with CCD cameras such as shot noise and pixel non-uniformity. Typically, shot-noise limited Hartmann sensors can measure tilts to within a few thousandths of a wave[30]. This high sensitivity results from the nature of the deflection measurements: since it is the relative position of the focal spots from the initial position that yields the tilt, slight misalignments and imperfections in the focal spot intensity profile are automatically subtracted from the measurement. We assume that the initial spot profiles and positions are well calibrated and misalignments are stationary. With care the Hartmann sensor can yield tilt measurements with sensitivity that may equal or exceed interferometric methods where sensitivity can reach several hundredths of a wave.

Accuracy of the detector is also subject to errors produced by the algorithms that determine focal spot locations from the intensity pattern recorded on the camera. Simulations of the tilt measurement accuracy of a 1-dimensional Hartmann sensor[33] in the presence of the electronic read noise variance of 1.4 mV (saturation = 1 V) and 13-μm pixel size of the inexpensive EG&G CCD cameras used in the

experiments show an RMS error in calculated spot location of less than 1 μrad for simple thresholded centroid-locating algorithms. A more sophisticated matched-filter spot-locating technique[32] has been found to show less sensitivity to errors due to finite pixel size than the centroid method. For the lenslet array focal length of 10 cm used in our system, lenslet diameter of 0.635 mm and laser wavelength of 633 nm, 1 μR angular deflection error corresponds to an approximate sensitivity of 0.001 waves. We verified this sensitivity using a novel spherical wave test[34] performed in our lab. In this test, best linear fits to the measured slope of a spherical wave of known curvature yielded an average experimental tilt sensitivity between adjacent lenslets of 0.6 μR. Further discussion of the 1D Hartmann sensor simulation is given in Section 5.

Additional sources of noise are the non-static room air disturbances and table vibrations, although these are minimized by floating the optical table and erecting screens around the table top. It is often difficult to separate and predict all environmental sources of noise. However, experimental tilt measurements were taken using the optical system shown in Fig. 2 without the jet turned on to measure the effect of the environment on the entire system. Many no-flow measurements were taken under varying ambient laboratory temperatures. These measurements yield an RMS noise tilt of approximately 5 μR, which corresponds to a sensitivity of 0.005 waves. We have found that the average RMS tilt signal from the flow field is approximately 30 μR with a center flow velocity of 5 m/s and a mean plenum temperature of 30 degrees C above ambient.

5. Flow field Characterization using the Hartmann sensor

Beam jitter measurements made from a small number of thin beams positioned in a line in the streamwise direction have been used previously[27,28] to determine the presence of organized, periodic vortical structures in jet flows. Temporal correlations between the temporal jitter signals from widely spaced detectors have been used to measure the coherence, size, velocity, and interaction activity of these vortical structures as well as the variation in these quantities with downstream distance. The submillimeter spatial resolution of the Hartmann sensors allow spatial as well as temporal mappings and correlations of flow structures to be produced in the cross-stream as well as the streamwise directions.

In this paper tilt measurements were taken in two orthogonal sensor orientations: streamwise and cross-stream. The cross-stream data was taken using a horizontal orientation of the linear Hartmann array located at a height of 2.5D above the nozzle exit. In this orientation, information is collected about the uniformity of the flow structure along a cross section of the flow perpendicular to the flow direction. Streamwise data was taken using a vertical orientation of the sensor, which is parallel to the convecting vortical train of the flow, centered in the flow at 2.5D. It is the streamwise orientation that most closely resembles the beam jitter geometry in the literature. However, the 40 subapertures of the Hartmann sensor provide 40 separate measurements of the jitter along a 1-inch streamwise line. The spatial resolution of the Hartmann sensor is 0.635 mm (the lenslet spacing). Its temporal resolution is 0.45 ms.

Figures 7(a) and (b) show deflection and wavefront data taken in the streamwise orientation. The slanted appearance to the structure in the deflection and wavefront data is due to the periodic convection of vortices along the array. The slope of the trajectories gives the convection velocities of the structure. The approximate slope of the trajectory pictured in Fig. 8 is 3.6 m/s, a reasonable convection velocity for the structures in a flow with a center velocity of 5 m/s.

Figures 8(a) and (b) show plots of deflection data and its corresponding wavefront taken using the cross-stream orientation of the sensor. These plots show a spatially resolved time-history of a horizontal cross section of the jet at a height of 2.5D. The wavefront is obtained by integrating the deflection data across the length of the array at each point in time.

Shown in Fig. 9 is the space-time correlation, $C(\xi_i, \tau_j)$, of the (a) streamwise and (b) cross-stream data graphed as a function of space and time difference variables, $\xi_i = i\Delta x$ and $\tau_j = j\Delta t$, respectively,

$$C(\xi_i, \tau_j) = \sum_{n=1}^{N} \sum_{m=1}^{M} \theta(x_n, t_m)\, \theta(x_n - \xi_i, t_m - \tau_j), \tag{4}$$

where N is the number of spatial samples along the length of the array spaced at an interval of $\Delta x = 0.635$ mm, and M is the number of time samples in each data set taken at time interval $\Delta t = 0.45$ ms. The i and j are integers.

A profile through the vertical axis of the 2D correlation taken at the time interval $\tau_j = 0$ (i. e., $C(\xi_i, 0)$) can be interpreted as the time-averaged spatial correlation of the data. Conversely, a horizontal profile, $C(0, \tau_j)$, through this 2D correlation at $\xi_i = 0$ can be interpreted as the temporal correlation of the data averaged over the length of the detector.

A measure of the average size of the convecting structures can be obtained from the width of the streamwise correlation along the horizontal or vertical axes. We can interpret the width of the correlation as a scale size without making an assumption about the convection velocity by considering the streamwise correlation along the vertical axis given by $C(\xi_i, 0)$. The best fit Gaussian to streamwise $C(\xi_i, 0)$ has a half-width, which we are using as the measure of correlation length, of 3.4 mm. The correlation length of the cross-stream $C(\xi_i, 0)$ is 2.8 mm indicating that cross-stream structures in the flow may be slightly smaller than streamwise structure, or that there may be a wider variety of structure in the cross-stream direction.

The slope of the line connecting the correlation peaks in the 2D streamwise correlation graph (Fig. 9 (a)) gives the average convection velocity. The measured slope is approximately 3.3 m/s in reasonable agreement with the previous measurement. The fact that the correlation peaks decrease in magnitude as the separations in time and space become large indicates that the signals decorrelate over distances over time and distance. In other words, the vortical structures have slightly different shapes, different evolution downstream and the periodicity of the structures is incomplete.

An indication of the periodicity of the vortical train is given by the correlation coefficients. Figure 10 shows the temporal correlation coefficient graphed as a function of the temporal separation between two frames of data, τ_j,

$$C(\tau_j) = \frac{\sum_{n=1}^{N} \theta(x_n, t_m)\,\theta(x_n, t_m + \tau_j)}{\sqrt{\sum_{n=1}^{N} \theta^2(x_n, t_m) \sum_{n=1}^{N} \theta^2(x_n, t_m)}}, \qquad (5)$$

where $x_n = n\,\Delta x$ is the position of the subaperture along the length of the Hartmann array and $\theta(x_n, t_m)$ is the spatial tilt signal from the 40 subapertures of the sensor taken at time t_m. This metric indicates how well the wavefront sensor measurement, over the entire array, correlates with another measurement taken at another point in time.

The streamwise correlation coefficient (Fig. 10 (a)) shows periodicity as might be expected from Fig. 7. In this orientation each vortical structure convects by all 40 subapertures along the sensor's streamwise oriented axis. Conversely, in the cross-stream orientation each structure convects by the detection plane only once. Thus, undersampled structures and variations in the structures along the width of the flow contribute to irregularities in the cross-stream correlation coefficient shown in Fig. 10 (b). However, cross-stream periodicity is still shown.

From this brief analysis, the average convection velocity and average vortical structure size across the 1" detector array can be inferred. The Hartmann sensor offers a way of taking high spatial resolution jitter data. Using all 40 measurements of the jitter per inch can yield the distribution of scale sizes as well as the distribution of convection velocities and how this distribution changes with downstream distance. Although this specific analysis is beyond the scope of this paper it is the subject of a forthcoming publication.[35]

6. Hartmann sensor simulation, tomographic simulation and system design.

The design of a multi-projection tomographic system (shown schematically in Fig. 2) has three basic elements: the number of projections, the number of samples (called lenslets or rays) in each projection and the focal length (or f-number) of the lenslets in the Hartmann arrays. The number of projections in the design determines the number of Hartmann sensors that are required to operate simultaneously. The number of samples and the lenslet f-number in the design determine how many subapertures each sensor must contain. The complete system design depends on instrumentation noise characteristics as well as flow parameters. The design presented here is based on the results of a 1D Hartmann sensor simulation and an analysis of computed tomographic (CT) reconstructions.

A Hartmann sensor spot-location-error simulation allow us to optimize the focal length of the lenslets under conditions similar to laboratory measurements. In the simulation, the intensity pattern (i.e., the lenslet focal spot intensity) impinging on a 2048-pixel CCD array is modeled as a sinc-squared pattern averaged over the finite area of each pixel. Detector noise, which slightly deforms the spots and causes error in the spot location algorithm, is modeled as a zero mean Gaussian distributed random process at each pixel that is uncorrelated from pixel to pixel. The variance of the noise is set to match laboratory observations of 0.15% of the average signal peak. Incoherent interactions between nearest neighbor spots are included in the simulation. Coherent interactions between the spots, which may be a significant source of noise, have not been included in this simulation. Since the experiments are run at high light levels photon noise is neglected. The exact position of each spot is

selected from a uniform random distribution of angular positions up to +/- 30 μR, a value chosen to match the flow tilt measurements. The length of the array is fixed at 1 inch.

Predicted sensor performance based on read noise is plotted as a function of lenslet focal length in Fig. 11 for sensors with 40, 64 and 128 lenslets per inch (LPI). It should be noted that the sensor measures spot deflections, that is, the difference between two spot position measurements. If we assume that the spot location error is uncorrelated between these two measurements, then the predicted tilt variance will be twice the spot position variance and the RMS spot position error is a factor of $\sqrt{2}$ higher than the values given in the plot. The curves in Fig. 11 show that the current laboratory Hartmann sensor system with 40 lenslets per inch and a focal length of 10 cm is near optimal with a read noise level of approximately 0.78 μR. This modeled sensor behavior agrees well with observed noise levels: actual measurements made over short time periods, when uncorrelated detector noise is expected to dominate and coherent effects are minimized, show RMS noise tilts of about 0.7 to 0.9 μR.

Predicted read-noise levels shown in Fig. 11 are input to a CT simulation to discern the effects of lenslet size and focal length on the quality of tomographic reconstructions. A model of a flow cross-section developed for the CT simulation is shown as the truth image in Fig. 13. In the CT simulation, projections are calculated by computationally propagating laser light through the cross-sectional model at specified angles. Noise is then added to the projections as an RMS error in the optical path difference (OPD). The OPD is calculated from tilt by integrating the tilt over the length of the array from both directions and averaging both results. For noise tilt at the ith lenslet given by θ_i, we may write the noise OPD as

$$OPD_{N+1} = \frac{d}{2}\left(\sum_{i=1}^{N}\theta_i\right) \qquad (6)$$

where d is the diameter of a lenslet, and N is the number of lenslets in the array. Equation (6) has 2 useful properties: it is zero mean and the OPD at each point i has the same error. Because the noise OPD is the sum of independent random variables the RMS noise OPD, σ_{OPD}, is given by

$$\sigma_{OPD} = \frac{d\sqrt{N}}{2}\sigma_\theta \qquad (7)$$

where σ_θ is the RMS noise tilt.

Three levels of noise tilt were considered in the simulation corresponding to no read-noise tilt, simulated levels of read-noise tilt illustrated by Fig. 11, and an estimate of a high-noise tilt case that may include the effect of coherent focal spot interactions. The corresponding RMS OPD errors for these cases for 40, 64 and 128 LPI sensors are shown in Table 1.

Table 1. Noise tilt and noise OPD levels.

LPI	Simulation		High-noise	
	RMS Tilt (μR)	RMS OPD (μm)	RMS Tilt (μR)	RMS OPD (μm)
40	0.64	0.0013	6.0	0.012
64	0.99	0.0016	6.0	0.0095
128	2.05	0.0023	6.0	0.0067

The resulting quality of image reconstructions from noisy data was assessed as a function of the number of projections used in the simulation and the number of samples (lenslets or rays) within each projection. Examples of tomographic reconstructions are shown in Fig. 12. Image quality is measured using RMS difference between the pixel values of the truth image and the reconstructed image over the entire image. The RMS error is graphed as a function of the spatial resolution of the projections in Fig. 13. From the figure it is evident that approximately 9 projections and 64 samples per projection are sufficient to reconstruct an image with 5.5% accuracy. It is interesting to note from Fig. 13(b) that although in the noiseless case the tomographic reconstruction improves as the number of rays increases, the 64 LPI reconstruction is actually more accurate than the 128 LPI in the presence of simulation noise. This behavior is due to the N dependence in Eq. (7). The optimal focal length corresponding to the 64 LPI sensor is approximately 4 cm (see Fig. 13).

This simplistic analysis of the tomographic simulation yields three important physical elements of the tomographic design: number of projections, number of samples per projection and the sensor focal length. An important quantity that is not determined by this analysis is the resolution of the tomographic imaging system. The resolution of the reconstruction process is a function of the number of projections, the number of samples per projection as well as the size and shape of the area to be reconstructed.[36] In order to capture relevant features in the flow-field cross section a resolution of at least 2 mm is desirable. Whether the system designed here can reproduce features of this size is at this time being determined using transfer function analysis.

The remaining consideration is the speed of the system. To capture the structure in the flow and its evolution it is desirable to operate the tomographic system at least 2000 frames per second. For 9 simultaneous projections each containing 2048 8-bit pixels a data rate of about 300 Mb per second is necessary.

7. Summary and continuing research

We have shown that 1D Hartmann sensing is a powerful technique for investigating the structure of flow fields. Although Hartmann sensing is closely related to the beam deflection techniques used in previous turbulence investigations, Hartmann sensing offers the advantages of controllable sensitivity and high spatial resolution. Plots of wavefronts as well as spatial and temporal correlations of a heated jet flow produced from Hartmann data are presented.

We have presented the design of a fast optical tomographic system that can be used to investigate organized structure in flows that may characterize a moving flow to a spatial resolution of 2 mm and a temporal resolution of 2 KHz. The tomography system design is based on the use of 1D Hartmann sensors. The acquisition of integrated optical phase data taken through the flow in several different directions simultaneously allows the structure to be tomographically imaged while also yielding information about the optical aberrations caused by the flow.

The noise and sensitivity characteristics of the Hartmann sensor were simulated and measured. Computed tomography was used with the sensor simulations to optimize the Hartmann lenslet size and focal length as well as to determine the number of projections necessary to produce an accurate image. We intend to improve the Hartmann sensor simulation by including coherent interactions between spots as an additional significant source of noise. To mitigate measured coherent effects we are developing apodized lenslet designs. Finally, development of a more sophisticated image quality metric for tomographic images is necessary to assess the resolution of the reconstructed images.

8. Acknowledgment

We would like to thank Dr. Daniel R. Neal for the use of the linear Hartmann sensor and software technology developed at Sandia National Laboratories in Albuquerque, NM.

9. References

1. H. E. Fielder, " Coherent structures in turbulent flows," Prog. Aerospc. Sci. **25**, 231-269 (1988).
2. P. E. Dimotakis, R. C. Miake-lye, and D. A. Papntoniou, "Structure and dynamics of round turbulent jets," Phys. Fluids **26**, 3185-3192 (1983).
3. S. C. Crow, and F.H. Champagne, "Orderly structure in jet turbulence," J. Fluid. Mech. **48**, 547-591 (1971).
4. G.L. Brown, and A. Roshko, "On density effects and large structure in turbulent mixing layers," J. Fluid. Mech. 64, 775-816 (1974).
5. E. Acton, " A modelling of large eddies in an axisymmetric jet," J. Fluid. Mech. **98**, 1-31 (1980).
6. D. Kyrazis, J. B. Wissler, D. D. B. Keating, A. Preble, K. P. Bishop, " Measurement of optical turbulence in upper troposphere and lower stratosphere," presented at SPIE OE-LASE 94 Meeting, 22-29 Jan 94, Los Angeles, CA.
7. F. Dadaudier, A. S. Gurvich, V. Kan, C. Sidi, " Middle stratosphere temperature spectra observed with stellar scintillation and in-situ techniques," COSPAR-92, paper C2-S2.09 accepted in Advances in Space Research, 1994.
8. A. S. Gurvich, "Scintillation spectra by observations of star occulatations by the Earth's atmosphere," Optica Atmosfery **2** (3), 239-245 (1989).
9. A. D. Kathman, L. Brooks, D. A. Kalin, and R. L. Clark," A time integrated image model for aero-optics analysis," AIAA paper 92-2793, AIAA and SDIO Annual Interceptor Technology Conference, Huntsville, AL (1992).
10. L. Chew, W. Christiansen, "Coherent structure effects on the optical performance of plane shear layers," AIAA J. 29, 76-80 (1991).
11. C. R. Truman, and M. J . Lee, " Effects of organized turbulence structures on the phase distortion in a coherent optical beam propagating through a turbulent shear flow," Phys. Fluids A 2, 851- 857 (1991).
12. B. Masson, J. B. Wissler, and L. McMackin, "Aero-optical study of a NC-135 fuselage boundary layer," AIAA 94-0277, 32nd Aerospace Sciences Meeting and Exhibit, Reno, NV (1994).
13. R. J. Santoro, H. G. Semerjian, P. J. Emmerman, and R. Goulard, "Optical tomography for flow field diagnostics," Int. J. Heat Mass Transfer 24, 1139-1150 (1981).
14. G. W. Faris, and R. L. Byer, "Three-dimensional beam deflection optical tomography of a supersonic jet," Appl. Opt. 27, 5202-5212 (1988).
15. R. Snyder, and L. Hesselink, "High speed optical tomography for flow visualization," Appl. Opt. 24 4046-4051 (1985); "Measurement of mixing fluid flows with optical tomography," Opt. Lett. 13, 87-89 (1988).
16. A. F. Gmitro, and G. R. Gindi, "Computed tomography videography: an electrooptical system for video-rate image reconstruction," Appl. Opt. 24, 4040-4045 (1985).

17. D. W. Watt, and C. M. Vest, "Turbulent flow visualization by intertferometric integral imaging and computed tomography," Experiments in Fluids 8, 301-311 (1990).
18. E. J. Beiting, "Fiber-optic fan beam absorption tomography," Appl. Opt. 31, 1328-1343 (1992)
19. S. R. Deans, The Radon Transform and Some of its Applications, (John Wiley and sons, 1983).
20. G. T. Herman, ed. , Image Reconstructions from Projections, Topics in Applied Physics v. 32 (Springer-Verlag, 1979).
21. W.-J. Yang, *Handbook of Flow Visualization*, (Hemisphere Publishing, New York, 1989), Ch. 20, "Optical tomography," L. Hesselink, p. 307.
22. D.Verhoeven, "Limited-data computed tomography algorithms for the physical sciences," Appl. Opt. **32**, 3736-3754 (1993).
23. R. Gordon, "A tutorial on ART," IEEE Transactions on Nuclear Science **NS-21**, 78-93 (1974).
24. G. T. Herman, L. B. Meyer, "Algebraic Reconstruction Techniques can be made computationally efficient," IEEE Trans. on Med. Imaging 12, 600-609 (1993).
25. R. K. Tyson, *Principles of Adaptive Optics* (Academic Press, Inc., Boston, 1991), Ch. 5.
26. D. R. Neal, T. J. O'Hern, J. R. Torczynski, M. E. Warren, and R. Shul, "Optical diagnostics in fluid and thermal flow," SPIE Proc. v. 2005, 194-203 (1993).
27. E. J. Jumper, and R. J. Hugo, "Optical phase distortion due to turbulent fluid density fields: quantification using the small-aperture beam technique," AIAA 92-3020 (1992).
28. G. T. Kalghati, "A study of coherent structures in axisymmetric jets using an optical technique," University of Southampton Report AASU-341 (1979); AIAA J. **18**, 225-226 (1980).
29. Wissler, A. Roshko,"Transmission of thin beams through turbulent mixing layers," AIAA 92-0658, June (1992).
30. A.A. Townsend, *The Structure of Turbulent Shear Flow*, (Cambridge University Press, 1980).
31. D. R. Neal, T. J. O'Hern, J. R. Torczynski, M. E. Warren and R. Shul, "Wavefront sensors for optical diagnostics in fluid mechanics: application to heated flow, turbulence and droplet evaporation," SPIE Proceedings, v. 2005 Optical Diagnostics in Fluid and Thermal Flow, 194-203 (1993).
32. D. Kwo, G. Damas, and W. Zmek, "A Hartmann-Shack wavefront sensor using a binary optic lenslet array," SPIE v. 1544 Miniature and Micro Optics: Fabrication and System Applications, 66-74 (1991).
33. R. Pierson and E. Chen, "Simulation of a one-dimensional Hartmann sensor," Technical Report (in preparation), Applied Technology Associates, Inc., Albuquerque, NM.
34. N. Clark, "Wavefront sensor system determination of Noise-Equivalent Tilt Angle Difference (NEΔTA)," Phillips Laboratory Technical Report (in preparation).
35. J. B. Wissler, K. Bishop, B. Masson, E. Chen, L. McMackin, "Convective flow structure and its evolution in a round turbulent jet," in preparation for submission to Appl. Opt. 1994
36. P. M. Joseph, R. D. Spital, and C. D. Stockham, "The effects of sampling on CT images," Computerized Tomography **4**, 189-206 (1980).

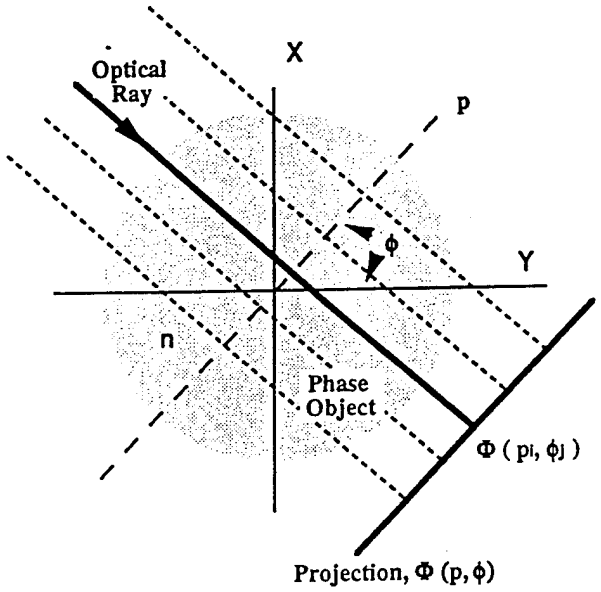

Fig. 1. A tomographic projection $\Phi(p, \phi)$ is made up of measurements along line p of the integrated optical path incurred by rays traveling in a certain direction, defined by angle ϕ.

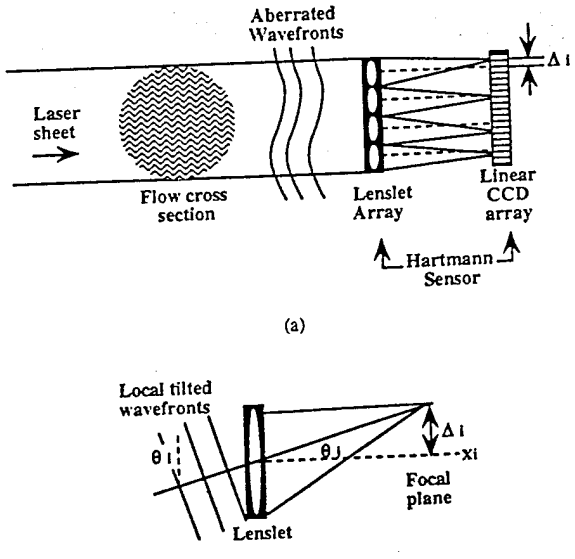

Fig. 2. (a) Linear Hartmann sensor schematic. An expanded laser sheet (propagating from left to right) propagates though a plane of the flow field that is perpendicular to the streamwise direction and impinges on an array of lenslets. Phase aberrations incurred by the beam show up as deflections, Δ_i, of the focal spots from their on-axis positions depicted by the dashed lines. The streamwise flow direction in this figure is out of the plane of the paper. (b) Close up of a single lenslet and a tilted wavefront showing the relation between the tilt θ_i and the measured focal spot deflection Δ_i.

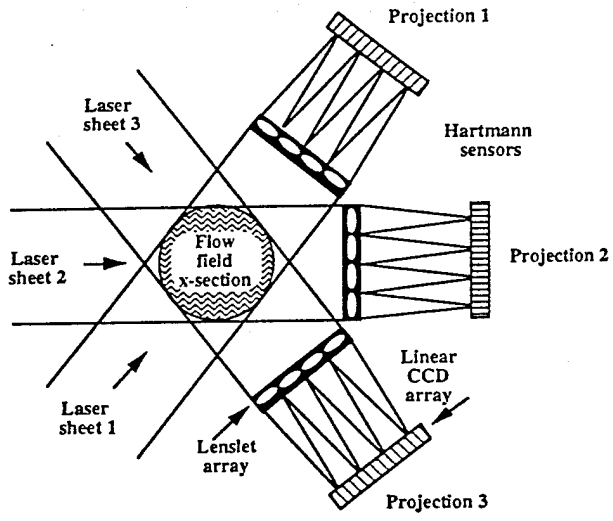

Fig. 3. Tomography requires the acquisition of phase measurements through the flow at many angles simultaneously. In the simple schematic shown here, three 1D measurements (called projections) are shown. Each of the projections measures the derivative of the optical wavefront as shown in Fig. 1. The spatial resolution of each projection is limited by the individual lenslet size, which is less than a millimeter.

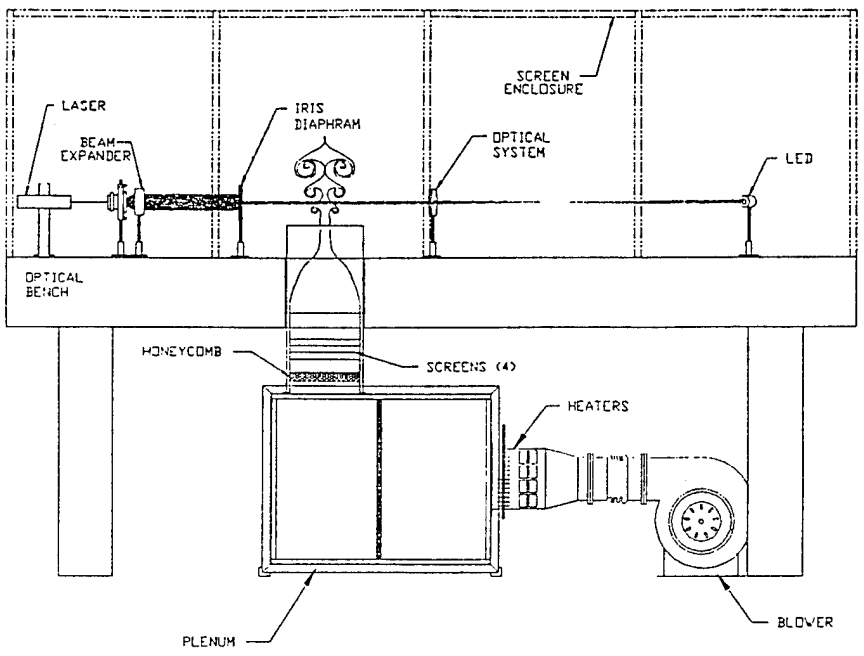

Fig. 4. Flow field generator schematic. Heated air is forced through a 1-inch diameter vertically oriented nozzle. The nozzle is located in a custom made hole at the center of an optical table so that the equipment for the optical investigation of the flow can be placed around the jet.

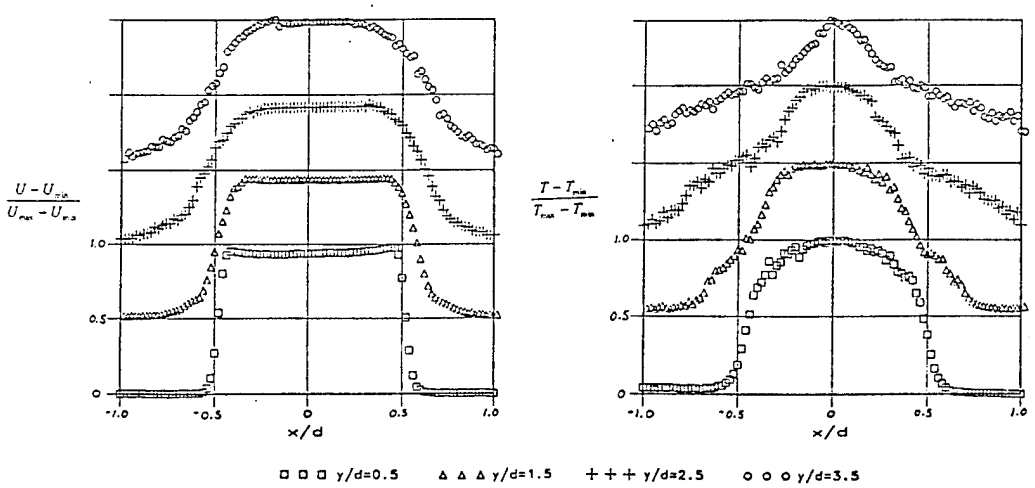

Fig. 5. (a) Radial mean velocity profiles and (b) Radial mean temperature profiles at four heights along the jet axis: 0.5, 1.5, 2.5, and 3.5 diameters (inches). x/d is the non-dimensional distance from the center of the jet. Scales on the ordinate are shifted for clarity.

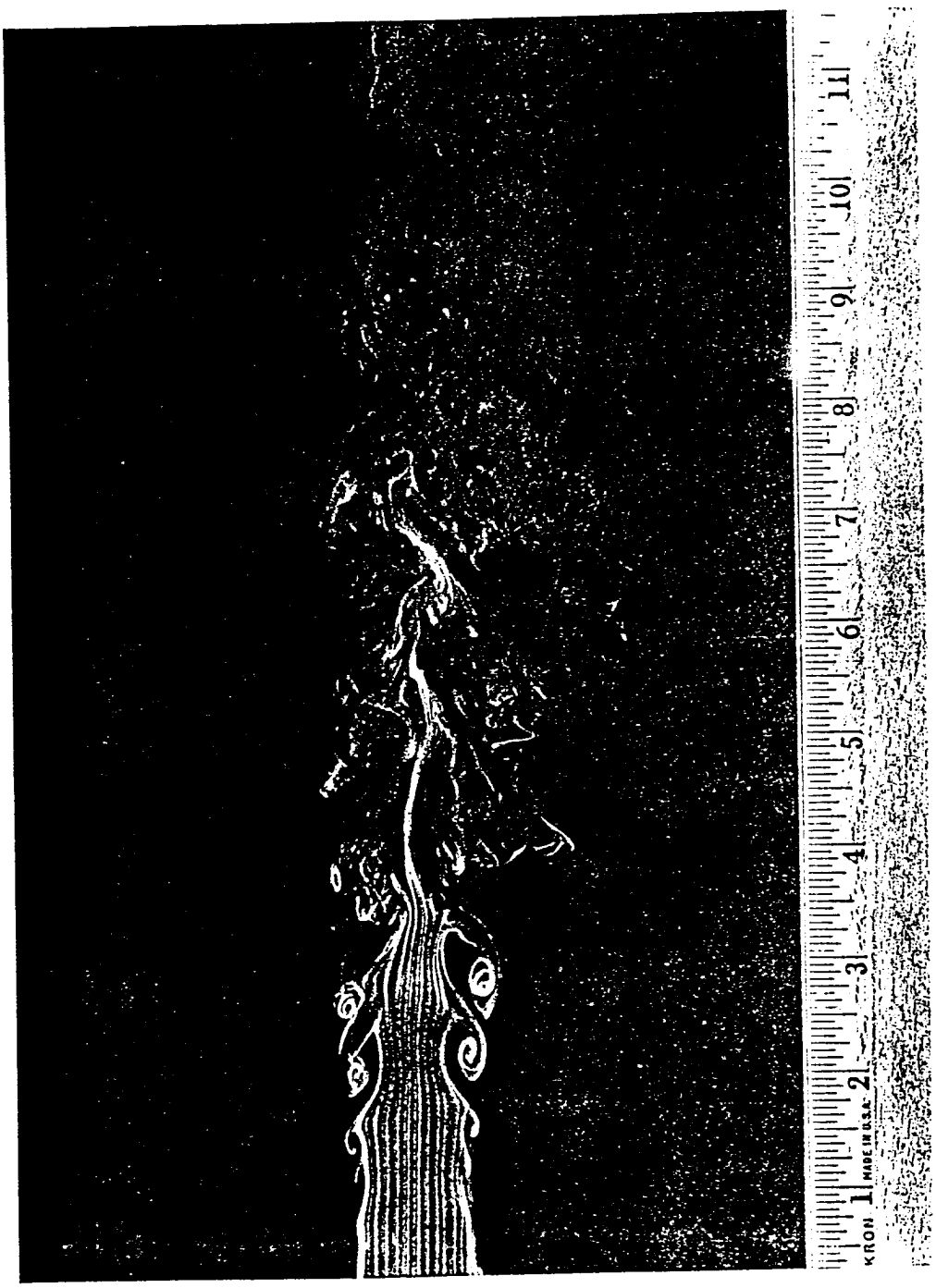

Fig. 6. Smoke wire visualization of the jet flow.

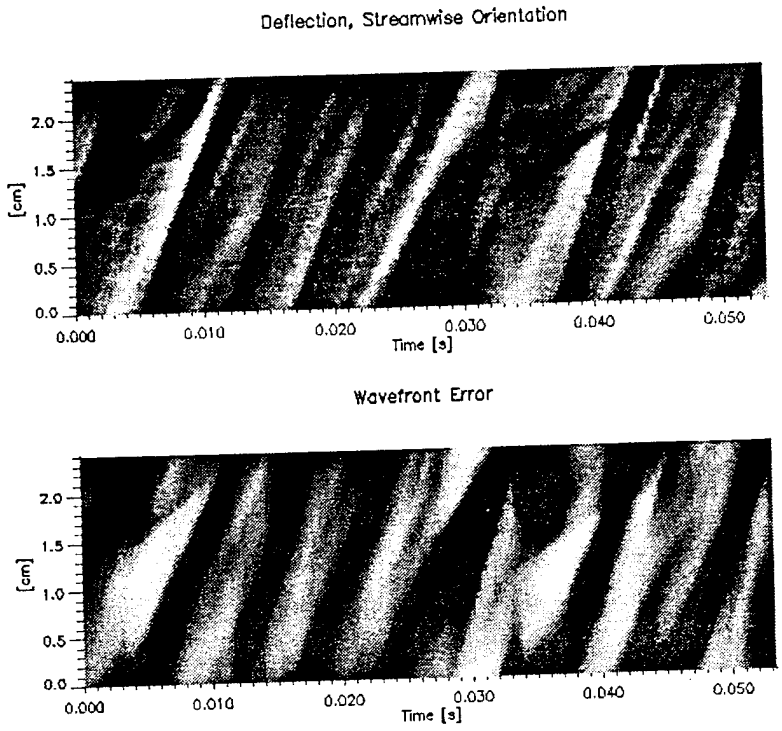

Fig. 7. (a) Deflection data and (b) wavefront acquired from a 1-inch long linear Hartmann sensor containing 40 subapertures in the streamwise orientation where the axis of the sensor is centered in the flow at a height of 2.5 inches and oriented parallel to the flow axis.

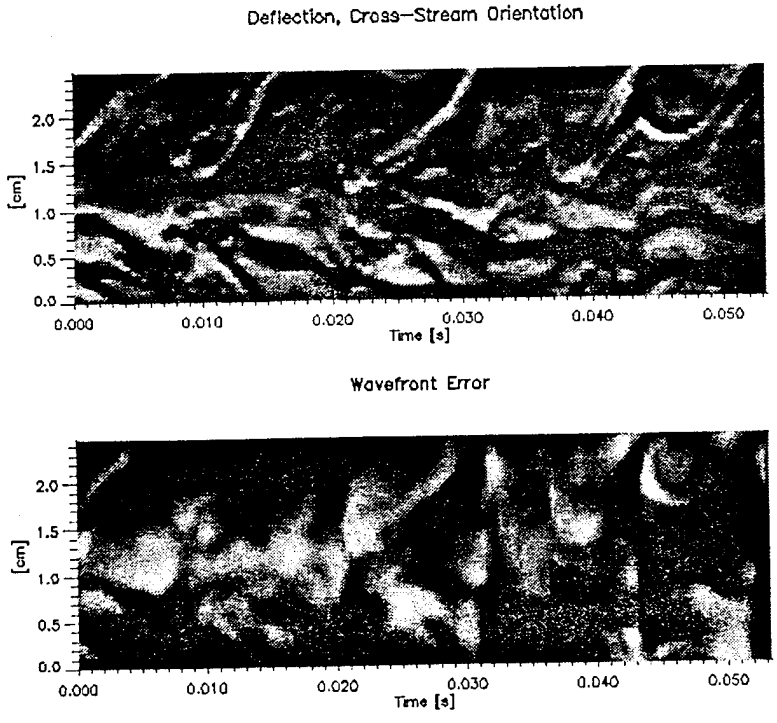

Fig. 8. (a) Deflection data and (b) wavefront acquired from a 1-inch long linear Hartmann sensor containing 40 subapertures in the cross-stream orientation where the axis of the sensor is oriented perpendicular to the flow axis at a height of 2.5 inches.

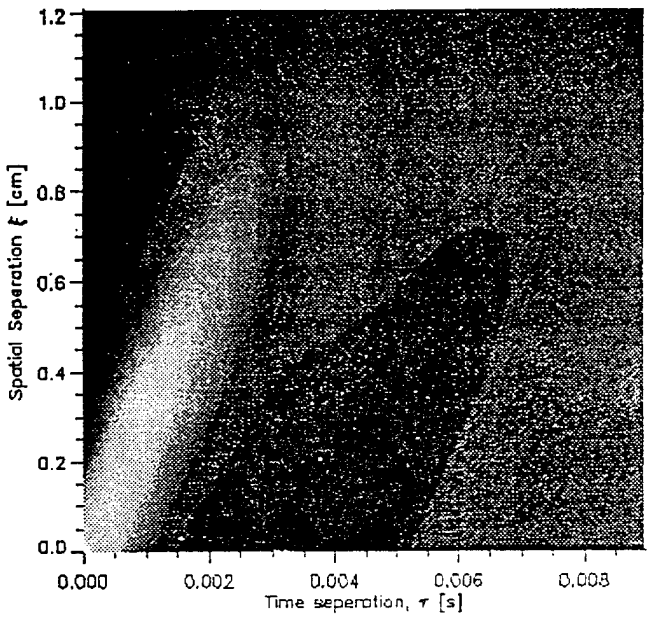

(a)

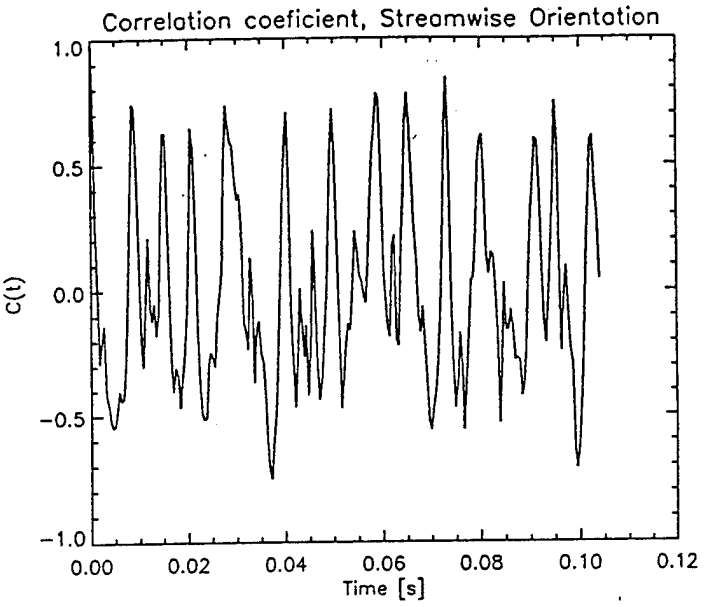

(a)

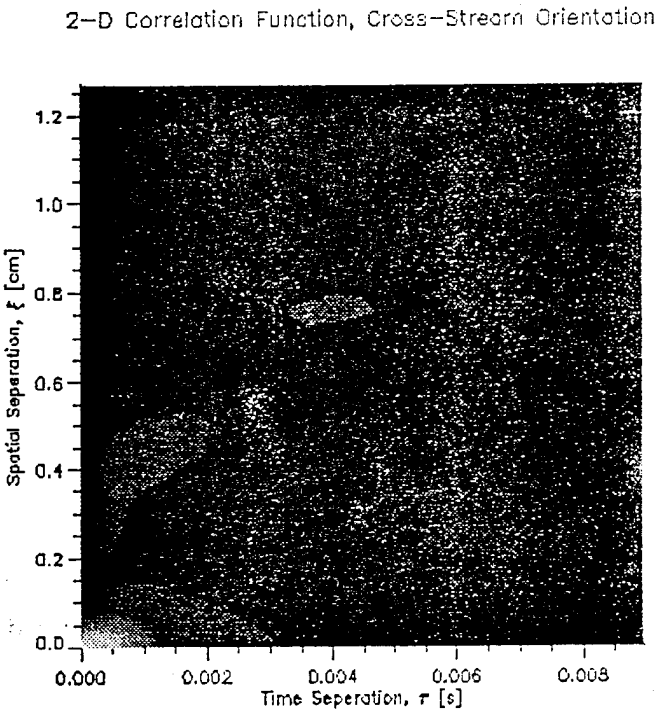

(b)

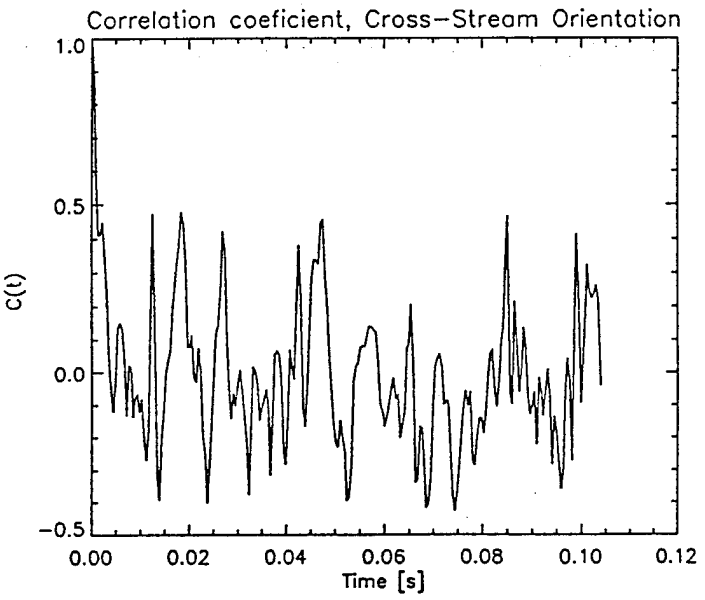

(b)

Fig. 9.(a) Spatial and temporal correlation of streamwise wavefront measurements. (b) spatial-temporal correlation of cross-stream data.

Fig. 10. Correlation coefficient in the (a) streamwise and (b) cross-stream orientation showing periodicity of flow structures.

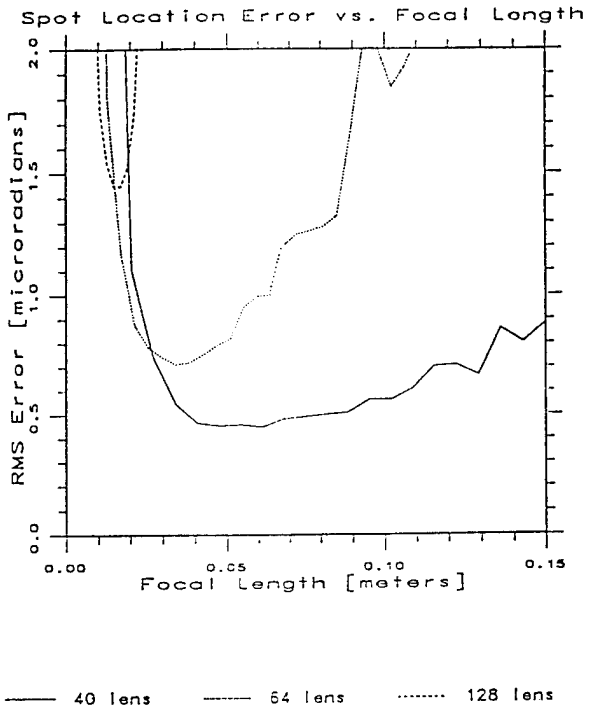

Fig. 11. Spot location error as a function of lenslet focal length.

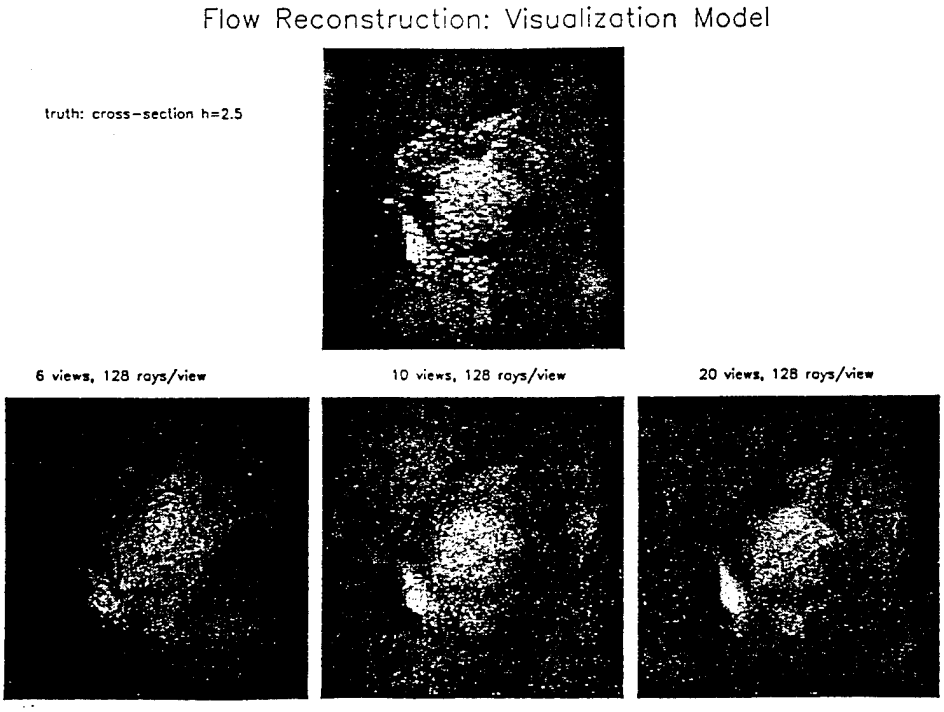

Fig. 12. Tomographic reconstruction of flow cross section using 6, 10 and 20 projections and 128 samples per projection.

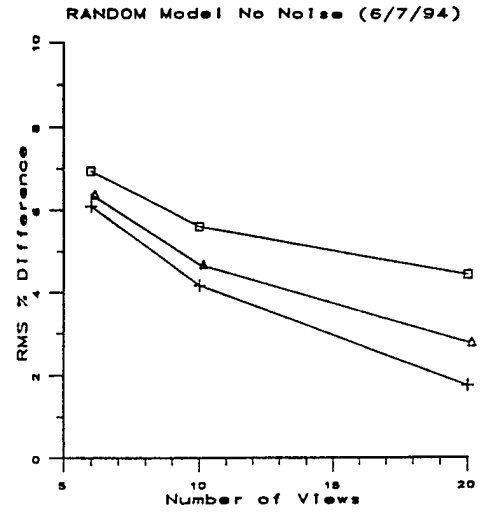

(a)

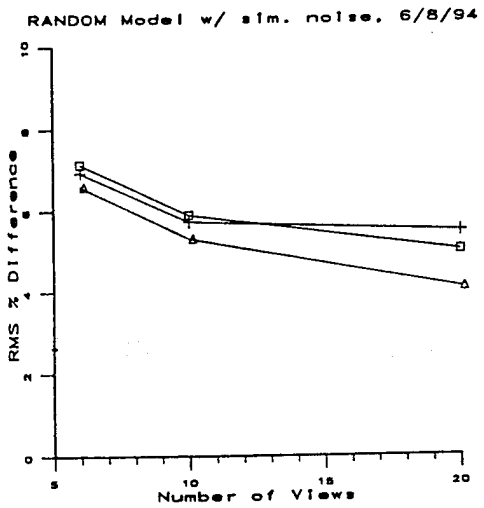

(b)

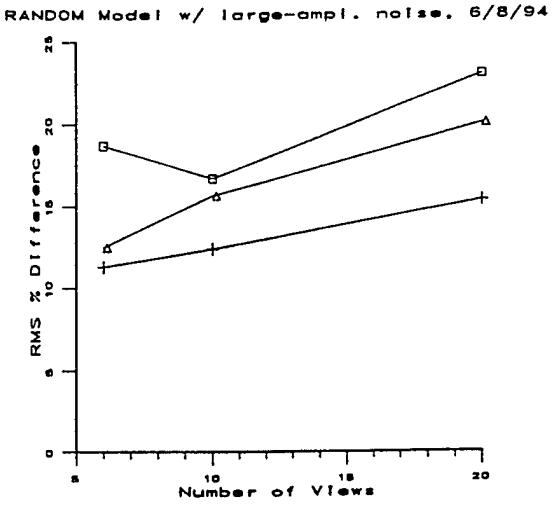

(c)

Fig. 13. Percent RMS error in the reconstructions as a function of the number of projections and the number of samples per projection for (a) noisless projections, (b) projections containing read-noise only and (c) high noise levels . ⊟-⊟-⊟ 40 rays △-△-△ 64 rays +-+-+ 128 rays